Discover Materials

RESEARCH Open Access

Comparative high-pressure structural and electrical transport properties study of thermoelectric $(Bi_{1-x}Sb_x)_2Te_3$ compounds

Chenxin Wei[1,2], Muhamed Dawod[2], Wenting Lu[1,2], Haikai Zou[1,2], Baihong Sun[1,2], Shiyu Feng[1,2], Qian Zhang[1], Zegeng Su[2], Hirokazu Kadobayashi[3], Martin Kunz[4], Bihang Wang[5], Azkar Saeed Ahmad[1,6], Yaron Amouyal[2*] and Elissaios Stavrou[1,2,6*]

*Correspondence:
Yaron Amouyal
amouyal@technion.ac.il
Elissaios Stavrou
elissaios.stavrou@gtiit.edu.cn

Full list of author information is available at the end of the article

Abstract

Thermoelectric $(Bi_{1-x}Sb_x)_2Te_3$ (BST-x) compounds, with x=0.2, 0.7 and 0.9, have been studied using synchrotron angle-dispersive powder x-ray diffraction in a diamond anvil cell up to 25 GPa (at room temperature). The results clearly indicate that all compounds of this study follow a similar structural evolution like the one of pure Bi_2Te_3 and Sb_2Te_3 under pressure. From the comparison between the critical pressures of the corresponding phase transitions, a clear trend of increasing critical pressure for the transition to the disordered solid-solution BCC phase was observed with the increase of Sb concentration. In the case of the BST-0.7, an extended stability of the solid-solution BCC phase up to, at least, 180 GPa was observed. Finally, electrical transport properties measurements under pressure for BST-0.7, document a reversible pressure-induced metallization above 12 GPa.

Keywords High-pressure, Thermoelectric materials, X-ray diffraction, Electrical properties

1 Introduction

Bi_2Te_3-Sb_2Te_3 compounds ($(Bi_{1-x}Sb_x)_2Te_3$, BST-x) have been extensively studied due to their outstanding thermoelectric properties at near-room temperature ranging from 300-500K [1–4]. The BST-x system exhibits full solubility. At ambient conditions, Bi_2Te_3, Sb_2Te_3 and BST compounds adopt the rhombohedral tetradymite crystal structure (space group $R-3m$(166)), formed by monoatomic sublayers of Bi/Sb, and Te atoms [5–7], independently of the relative concentration of Bi and Sb. The quintuple layers of Te-Bi(Sb)-Te-Bi(Sb)-Te are stacked in a sequence along c-axis direction [8, 9].

The high-pressure studies of Bi_2Te_3 and Sb_2Te_3 end members were motivated mainly by the possibility of using pressure to improve their higher thermoelectric conversion efficiency [10–12] and the increasing interest of the superconducting phase [13–16]. Bi_2Te_3 and Sb_2Te_3, exhibit, at least, three phase transitions under pressure. Zhu *etal.* [17]

clarified that Bi_2Te_3 transforms from the rhombohedral $R-3m$(six-fold coordination) phase (α-Bi_2Te_3 or phase I) to a monoclinic *C*2/*m* (seven-fold coordination) phase at 8 GPa (β-Bi_2Te_3 or phase II) and then to a *C*2/*c* (eight-fold coordination) phase at 14 GPa (γ-Bi_2Te_3 or phase III). At higher pressures, Bi_2Te_3 adopts a disorder solid-solution body-center cubic (BCC, A2) $Im-3m$ structure (phase IV), with a 40% and 60% occupancy of the 2a Wyckoff Position (WP) for Bi and Te atoms, respectively [17, 18]. An identical structural evolution was concluded for Sb_2Te_3 [19, 20], albeit with slightly different critical pressures. It is noteworthy, that the disordered BCC structure for Sb_2Te_3 appears at pressure above 20 GPa [19].

Studies on the structural evolution of $Bi_{1-x}Sb_xTe_3$ compounds under pressure are extremely limited. Indeed, Bai *etal.* [21] studied $Bi_{0.5}Sb_{1.5}Te_3$ (BST-0.75) only inside the pressure stability range of the ambient-conditions phase, <10 GPa. Jacobsen *etal.* [5], studied $BiSbTe_3$ (BST-0.5) up to 18 GPa, and a phase transition was observed at $\approx$ 7 GPa. However, the indexing of the high-pressure phase was not the one concluded by more recent studies on Bi_2Te_3 and Sb_2Te_3.

Motivated by the above, we have performed a detailed comparative $in-situ$ synchrotron angle-dispersive powder x-ray diffraction (ADXRD) study of three different BST-x compounds with x=0.2, 0.7 and 0.9, up to 20+ GPa. The selection of these compositions was made in order to scan the compositional range between low and high Sb concentration, with specific focus on x=0.7, see discussion in electrical measurements results. Our main motivation was to explore the structural evolution under pressure as a function of varying Sb concentration. Our results document that the three BST compounds follow the same phase sequence with the pure Bi_2Te_3 and Sb_2Te_3 under pressure, without any noticeable effect of the Sb concentration on the critical pressures for the first two phase transitions. On the other hand, it is apparent that the increase in the Sb concentration subsequently increases the critical pressure of the BCC phase formation.

In the case of BST-0.7, our study was extended to $\approx$ 180 GPa, with the aim of exploring the stability of the BCC phase under Mbar pressures. Surprisingly, we observe that the BCC solid-solution phase remains stable up to the highest pressure of this study. Finally, for the same BST-0.7, $in-situ$ electrical transport measurements as a function of pressure and temperature were performed. A clear indication for metallization was observed above $\approx$ 12 GPa.

2 Experimental methods

2.1 Materials Synthesis

$(Bi_{1-x}Sb_x)_2Te_3$ (BST-x) specimens with nominal composition x = 0.2, 0.7 and 0.9 were synthesized from pristine Bi granules (99.5%, LABORATORY REAGENTS & FINE CHEMICALS®), Te ingots (99.99%, STREM CHEMICALS®), and Sb granules (99.999%, ALFA AESAR ®), mixing them in the appropriate molar ratios to obtain these stoichiometric compositions. The pristine elemental granules were loaded into quartz ampoules, evacuated to 10^{-5} Torr, and sealed during the pumping process using the EXPT Pumping station (Edwards). The sealed ampoule were subsequently heated to 1123 K at 55 K/h for melting in a vertical programmable tube furnace (VECSTAR, UK). The melting procedures was completed after soaking for ca. 500 min. The ampoules were cooled down to RT at 55 K/h. This procedure yielded $(Bi_{0.8}Sb_{0.2})_2Te_3$, $(Bi_{0.3}Sb_{0.7})_2Te_3$ and $(Bi_{0.1}Sb_{0.9})_2Te_3$, ingots through solidification [4].

These ingots were grounded using a mortar and pestle and sieved at 56 μm powder (Haver test sieve with stainless steel wire cloth of 56 μm, HAVER & BOECKER). The fine powders were loaded into a 13.5 mm dia. stainless steel die and HP at 375 ^{o}C under 86 MPa for 1 h, then slowly cooled down to RT. The HP process will be conducted under flowing high-purity Ar (99.999%). The elemental composition was further examined using energy dispersive X-ray spectroscopy (EDX) measurements based on the Bi-Mα, Te-Lα, and Sb-Lα spectral lines collected using a 10 kV electron beam, see Fig. S1 and Table S1. The results confirmed that the difference between the measured (x=0.22±0.01, 0.71±0.01 and 0.89±0.01) and the nominal x values (0.2, 0.7, and 0.9) are inside the experimental uncertainty of the EDX measurements.

2.2 High pressure studies

A BX-80 type diamond anvil cell (DAC) with 400 μm diameter diamond culets was used for the high-pressure experiments. A Rhenium foil pre-indented to $\approx$ 50μm with a central hole diameter of $\approx$ 130 μm was used as gasket. Samples were loaded near the center of the sample chamber, along with a ruby chip and gold used as pressure markers, at the side. The shift of the ruby line [22] and the EOS of gold [23] were used to determine the pressure *in-situ*. Neon (Ne) was used as pressure transmitting medium (PTM) which is capable to maintain hydrostatic environment up to above 20 GPa [24], and loaded with a gas loader. For the study of BST-0.7 up to 180 GPa, beveled 100 μm diameter diamond culets were used and a Rhenium foil pre-indented to $\approx$ 30μm with a hole of 40μm in diameter was used as gasket.

2.2.1 X-ray Diffraction

X-ray diffraction (XRD) measurements at ambient conditions were performed with the Cu Kα_1 (λ=1.540598Å) X-ray line (Rigaku MiniFlex, Tokyo, Japan) to identify the starting crystal structures, see Fig. S2. The results confirm that all BST specimens adopt the rhombohedral tetradymite $R-3m$ crystal structure under ambient conditions, without any trace of impurity.

A Dectris Pilatus3 S 1M Hybrid Photon Counting detector was used at the Advanced Light Source, Lawrence Berkeley National Laboratory, Beamline 12.2.2. The spot size of the X-ray probing beam was focused to about 10 x 10μm using Kirkpatrick-Baez mirrors. More details on the XRD experimental setups are given in Kunz *etal.* [25]. At SPring-8, beamline BL10XU, a Flat Panel X-ray Detector (Varex Imaging, XRD1611 CP3) was used and the X-ray probing beam spot size was focused to approximately 10 x 10μm using compound refractive lens. More details on the SPring-8 XRD experimental setups are given in Hirao *etal.* [26]. At Beamline P02.2 at DESY, the X-ray probing beam were focused to a spot size of 2 x 2 μm at the sample using Kirkpatrick-Baez mirrors and a PerkinElmer XRD 1621 flat-panel detector was used to collect the diffraction images of sample.

The integration of powder diffraction patterns to produce scattering intensity versus 2θ diagrams and initial analysis were performed using the DIOPTAS program [27]. Calculated XRD patterns were produced using the POWDER CELL program [28] for the corresponding crystal structures according to the EOSs determined experimentally in this study and assuming continuous Debye rings of uniform intensity. XRD patterns indexing has been performed using the DICVOL program [29] as implemented in the

FullProf Suite. Rietveld refinements were performed using the $GSAS-II$ software [30].

2.2.2 Electrical measurements

In-situ high-pressure electrical resistance measurements for BST-0.7 were performed using the standard four-point probe method [R_1, R_2]. A T301 stainless steel gasket was first indented and a hole was drilled with a diameter of 300 μm. Cubic boron nitride (cBN) insulation powder was used to fill the hole and cover the steel to minimize its influence on the electrical measurement. After compressing cBN to ≈20 GPa, a smaller hole was drilled in the center with ≈150 μm in diameter. The rest of the gasket was covered with an epoxy insulating layer to further protect the electrode leads from the metallic gasket. Four electrodes were cut from a Pt foil and used for the electrical connection with the specimen.

The sample chamber was fully filled with the specimen, as a fine powder form, along with a small ruby chip at the center of the anvil opposite to the electrodes, for pressure determination. No PTM was used during the measurement because it would permeate the space between the powder specimen and the electrodes and interfere with their electrical contact under pressure. The sample and the Pt probes were pressurized to about ≈ 2 GPa in the DAC to achieve full electrical contact. A heating plate was used to heat the DAC and the temperature was measured with a thermocouple attached to the gasket near the sample chamber. At each temperature step, the measurements were taken >10 mins after reaching and stabilizing the desired temperature, to ensure thermal equilibrium inside the DAC.

3 Results

3.1 X-ray Diffraction

3.1.1 X-ray Diffraction of BST-0.2,0.7 and 0.9 up to 20–25 GPa

XRD patterns of the BST specimens of this study at selected pressures are shown in Figure 1. A slight deviation of the Bragg peaks relative intensities between the ambient pressure XRD patterns (Fig. S2) and the ones at initial compression is attribute to the difference between the experimental setups used for the relevant XRD measurements. In details, macroscopic powder specimens were used for for lab based XRD, while few-μm sized XRD beams were used for the high-pressure XRD diffraction that is, as normally expected, more prone to the effects of slight preferred orientations. All BST compounds remain in the rhombohedral phase (phase I) from ambient pressure up to ≈ 8–10 GPa. Above this pressure, a clear phase transition was observed, based on the gradual appearance and disappearance of Bragg peaks, towards the first high pressure phase (phase II). The coexistence of phase I and phase II is apparent up to 2–3 GPa above the first indication of the appearance of phase II. Above this pressure only the peaks of phase II can be detected. Above ≈ 15 GPa, another phase transition is evident towards the second high-pressure phase, phase III. As in the case of the Phase I → Phase II transition, Phases II and III also coexist for a certain pressure range. However, a clear increase of the pressure range of the co-existence is observed with increasing concentration of Sb. At even higher pressures, new Bragg peaks appear for BST-0.2 and BST-0.9, above 17.2 and 23 GPa, respectively; see arrows in Fig. 1(a) and (c). This is attributed to the third high-pressure phase IV (BCC, $Im-3m$ structure) that coexists with phase III for BST-0.2

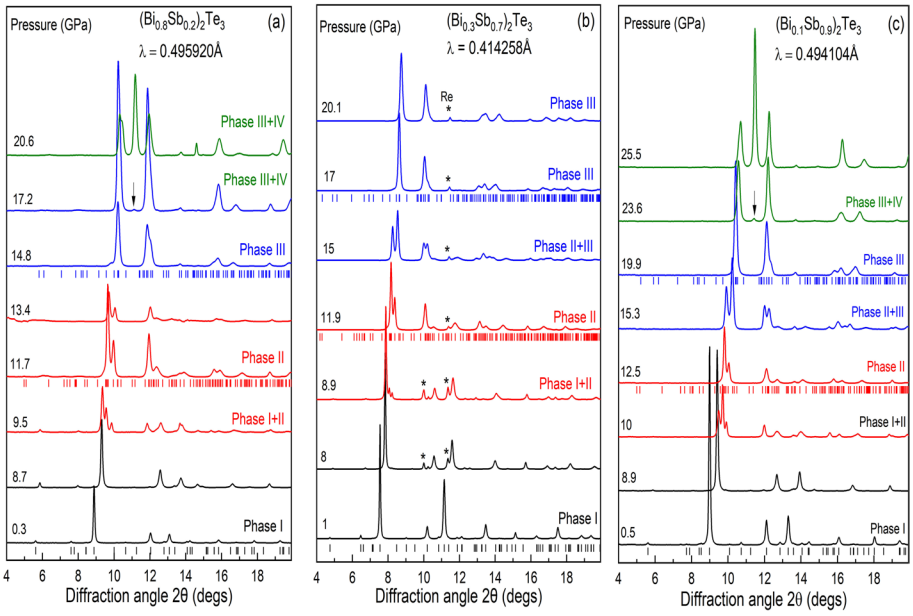

Fig. 1 XRD patterns of (**a**) BST-0.2, (**b**) BST-0.7 and (**c**) BST-0.9 at selected pressures. The peaks marked with asterisks originate from Re gasket material. The relevant predominant phases, $R-3m$(Phase I), *C*2/*m* (Phase II) and *C*2/*c* (Phase III) are noted with different colours. The arrows in (**a**) and (**c**) denote the first appearance of the strongest peak (1 1 0) of the BCC phase (phase IV). The corresponding X-ray wavelengths are noted inside the panels.

and BST-0.9 up to the highest pressures of this study. In contrast, no indication of phase IV is observed for BST-0.7 up to 20 GPa.

A more detailed comparison of the high-pressure phases reveals that the high-pressure phases II and III are identical in all BST specimens; see Fig. S3. Moreover, both phases II and III can be indexed with the previously reported Phase II (space group *C*2/*m* (12), Z=4) and phase III (space group *C*2/*c* (15), Z=4) monoclinic phases of Bi_2Te_3 at similar pressures [17]. Thus, we conclude that all the BST specimens of this study qualitatively follow the same structural evolution, including the co-existence of phases pressure ranges, under pressure with Bi_2Te_3, *i.e.* rhombohedral $R-3m$(phase I) $\rightarrow$ monoclinic *C*2/*m* (phase II) $\rightarrow$ monoclinic *C*2/*c* (phase III)$\rightarrow$ disordered BCC (phase IV). The reader is referred to the bar diagram in Fig. 2 for a detailed account of the critical pressures and stability pressure ranges for the observed phase transitions and phases.

From the relevant Rietveld refinements of the XRD patterns, see Fig. S4, using the crystal structures mentioned above, the experimental lattice parameters and cell volumes were determined and are plotted as a function of pressure in Fig. 3 and listed in Table 1. From the data of Fig. 3(d)-(f), the bulk modulus *B* and its pressure derivative *B'* were determined by fitting a third-order Birch-Murnaghan [31] Equation of State (EOS), Eq. 1, to the experimental data, see Table 1.

$$P=\frac{3}{2}B_{T_0}\left[\left(\frac{V_0}{V}\right)^{\frac{7}{3}}-\left(\frac{V_0}{V}\right)^{\frac{5}{3}}\right]\times\left\{1+\frac{3}{4}\left(B'_{T_0}-4\right)\left[\left(\frac{V_0}{V}\right)^{\frac{2}{3}}-1\right]\right\} \quad (1)$$

3.1.2 X-ray Diffraction of BST-0.7 up to Mbar pressures

Aiming to explore the pressure stability range of the disordered solid-solution BCC phase, BST-0.7 was pressurized up to 180 GPa. Part of our motivation was to explore

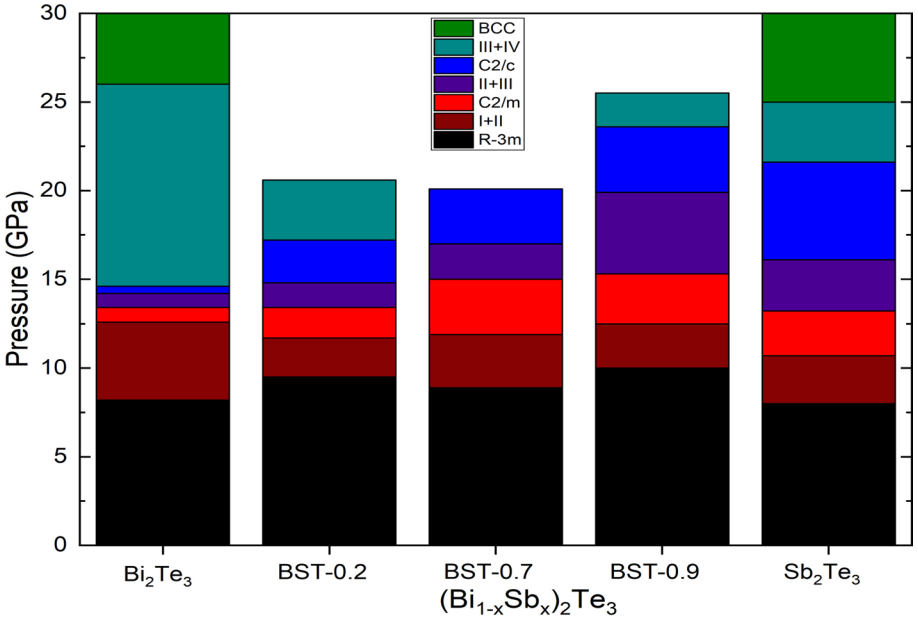

Fig. 2 Bar diagram showing the pressure stability intervals of the different structural modifications (Phase I ($R-3m$), Phase II ($C2/m$), Phase III ($C2/c$) and phase IV ($Im-3m$) of BST compounds and Bi_2Te_3 and Sb_2Te_3 end members. The data for Bi_2Te_3 and Sb_2Te_3 are adopted from Ref. [17] and Ref. [19], respectively.

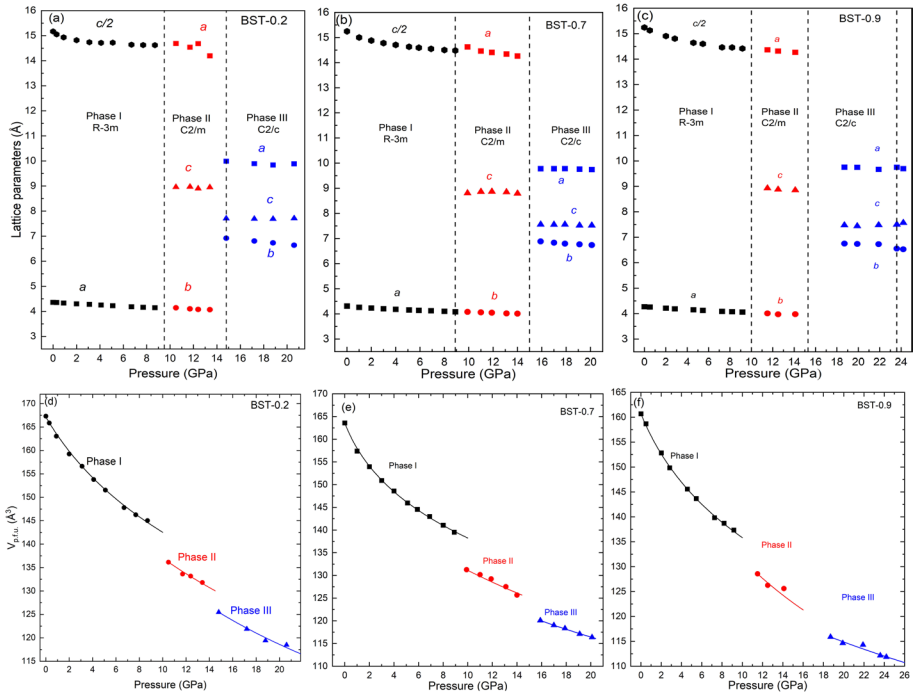

Fig. 3 Pressure dependence of the lattice parameters and cell volume per formula unit of (**a**), (**d**) BST-0.2, (**b**),(**e**) BST-0.7 and (**c**),(**f**) BST-0.9 as a function of pressure. The vertical dashed lines indicate the critical pressures of the phase transitions. The solid curves in (**d**),(**e**) and (**f**) are 3^{rd} order Birch-Murnaghan EOSs fitted to the experimental data.

Table 1 Experimental structural parameters of BST-0.2, 0.7 and 0.9 at selected pressures: space group (SG), number of formula units in the unit cell Z, lattice parameters, cell volume per formula unit V_{pfu}, bulk modulus *B* and its pressure derivative *B′* (as determined by fitting a 3^{rd} order Birch-Murnaghan EOS [31] to the experimental data) at the onset pressure.

P (GPa)	SG	Z	a (Å)	b (Å)	c(Å)	V_{pfu}(Å^3)	B (GPa)	B′
					BST-0.2			
Ambient	R-3m	3	4.359	4.359	30.506	167.316	39(4)	6.0 (0.4)
0.9	R-3m	3	4.351	4.351	30.341	165.797		
10.5	C2/m	4	14.688	4.141	8.958	136.151	79.4 (4.9)	4 (fix)
14.8	C2/c	4	9.991	6.918	7.706	125.471	82.5 (4.6)	4 (fix)
					BST-0.7			
Ambient	R-3m	3	4.303	4.30	30.430	162.638	22.9 (10)	13.5 (1.1)
3	R-3m	3	4.206	4.206	29.563	150.981		
14	C2/m	4	14.361	4.007	8.781	126.306	95 (6)	4 (fix)
20.1	C2/c	4	9.692	6.737	7.574	116.181	125.3 (1.6)	4 (fix)
					BST-0.9			
Ambient	R-3m	3	4.272	4.272	30.390	160.701	29.1 (2.0)	8.7 (1.2)
0.5	R-3m	3	4.260	4.260	30.264	158.551		
12.5	C2/m	4	14.319	3.974	8.879	126.269	69 (8)	4 (fix)
19.9	C2/c	4	9.749	6.738	7.440	114.632	147 (11)	4 (fix)

the effect of solid-solution, as opposed to the ordered B2 CsCl-type phase, to the pressure stability of the BCC phase. The B2 phase of NaCl remains stable up to $\geq$300 GPa [32, 33], while it is predicted to transform to an orthorhombic oC8 phase above 325 GPa [34]. On the other hand, CSI with much heavier and bigger elements, that adopts the CsCl-type structure under ambient conditions, has been reported to transform to an orthorhombic structure already at 45 GPa, and finally transform to an HCP-like structure at higher pressures [35, 36].

The XRD results of this study indicate that BST-0.7 remains in the BCC phase up to, at least, 180 GPa, see Fig. 4. For comparison, from previous studies it has been established that Bi remains in the BCC phase up to at least 220 GPa [37]. On the other hand, the BCC phase of Te transforms to the FCC phase at 99 GPa, and the FCC phase remains stable up to, at least, 330 GPa [38]. Finally, Sb adopts a BCC structure at 28 GPa, that remain stable up to 43 GPa [39]. According to Ref. [17], pressure results in a substantial Bi→Te charge transfers, resulting in an enhanced HP ionicity of the BCC phase of Bi_2Te_3. Thus, the extended stability of the BCC phase could presumably be attributed to this enhanced ionicity that stabilizes the BCC phase. A similar scenario was determined for the extended stability of the α-Mn phase, above the pressure that the HCP phase becomes energetically favorable [40].

3.2 Electrical measurements

The electrical resistance of BST-0.7 as a function of pressure, at room temperature, is shown in Fig. 5(a), for both the compression and decompression runs. Our main motivation for studying the electrical properties of BST-0.7 under pressure was our observation that, at ambient pressure, BST-0.7 shows an almost temperature-independent conductivity, in contrast to the clear semiconducting and metallic behavior of BST-0 (Bi_2Te_3) and BST-1 (Sb_2Te_3), respectively, see Fig. S5 [41]. Upon initial compression, the resistance rapidly decreases, reaching an almost constant value above $\approx$ 11–12 GPa. Such a pressure-dependent behavior of the resistance is attributed to a pressure-induced semiconductor to metal transition [42]. A similar pressure dependence of the electrical

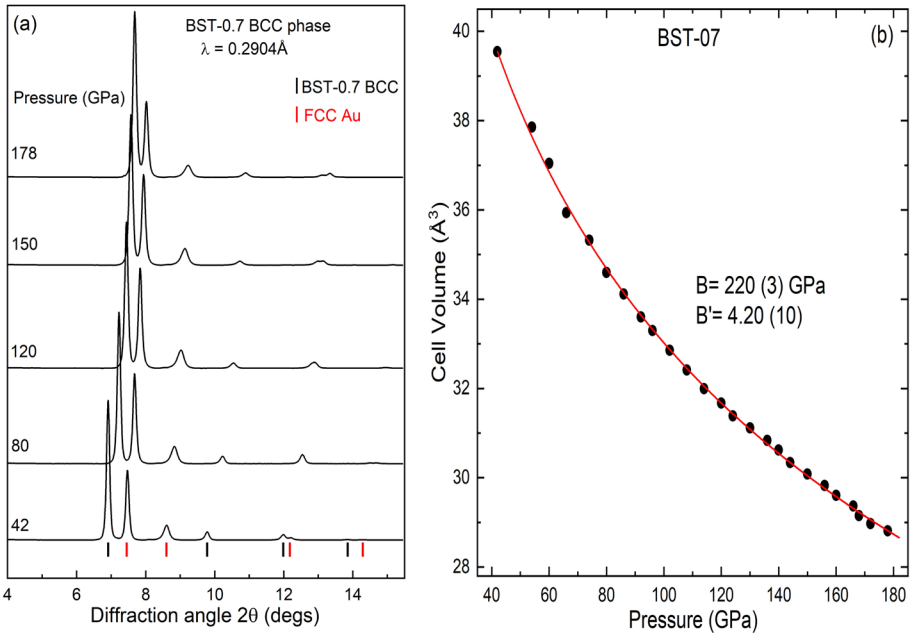

Fig. 4 (**a**) XRD patterns of BST-0.7 at selected pressures up to 178 GPa. The asterisks denote the Bragg peaks from Au (pressure marker). (**b**) Pressure dependence of the BCC cell volume of BST-0.7. The red solid curve is a 3^{rd} order Birch-Murnaghan EOS [31] fitted to the experimental data. The determined bulk moduli at the onset pressure are also given.

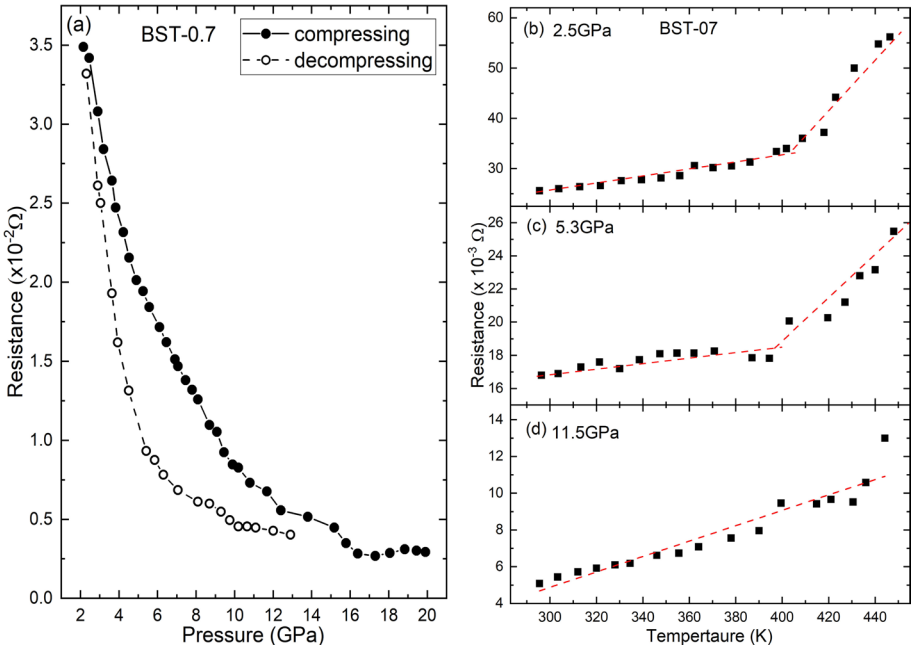

Fig. 5 (**a**) Electrical resistance of BST-0.7 as a function of pressure, at room temperature, under compression (solid symbols) and decompression (open symbols). Electrical resistance of BST-0.7 as a function of temperature at (**b**) 2.5 GPa, (**c**) 5.3 GPa and (**d**) 11.5 GPa. The dashed red lines are guides to the eye, see text for details.

resistivity was also observed in the case of pure Bi_2Te_3 [43]. Upon decompression, the resistance starts to increase around 6 GPa, and reaches almost the same, with initial compression, value at near ambient pressure with a hysteresis of ≈ 5–6 GPa. We note that in the electrical measurements no PTM was used and as a result non-hydrostatic

conditions are expected, that in general tend to shift the relevant phase transitions towards lower pressures [44]. Thus, a direct comparison with the phase diagram established by XRD measurements under hydrostatic conditions is not possible. However, from pervious studies on similar materials, it is established that no considerable deviation was found when comparing the results with and without PTM [17, 43, 45]. As a result, the non-hydrostatic conditions in electrical measurements do not affect our conclusion about the pressure-induce metallization of BST-0.7.

To confirm the pressure-induced metallization, we performed high-temperature electrical measurements at different pressures, see Figs. 5(b)-(d). For each heating run, the pressure was measured before and after each heating cycle, without any noticeable change of pressure when returning to room temperature. We note that, because of different experimental runs, and the fact that resistance is not an intrinsic property of the sample, comparison between absolute resistance values between runs is challenging. However, the temperature dependence of the resistance (metallic character) is of major importance. At lower pressures of 2.5 and 5.3 GPa, the resistance remains relatively constant up to about $\approx$ 400 K, an indicative of a material with very narrow band-gap, and then linearly increases with temperature showing metal like response. On the other hand, at 11.5 GPa, the resistance increases monotonically with temperature, highlighting the metallic character of the material at this pressure from room temperature. We note that, although challenging to establish a definite crossover temperature, the transition from narrow-band-gap $\rightarrow$ metallic character appears to occur at lower T for 5.3 GPa than 2.5 GPa; see dashed red lines in Figs. 5(b) and (c).

4 Discussion

4.1 Pressure dependence of the *c*/*a* axial ratio in the ambient phase of BST-*x*

In previous high-pressure studies of the ambient phase of Bi_2Te_3, a crossover of the pressure dependence of the c/a axial ratio was observed [46, 47]. In details, c/a initially decreases, as expected based on weaker van der Waals interlayer (c-axis) bonding, followed by an increase above 2.5–3.5 GPa. Polian *etal.* [46], attributed this trend to an electronic topological transition (ETT), that mainly affects the intralayer electronic distribution of the strong ionocovalent bonds, rendering the a-axis more compressible. The same crossover behavior of the c/a ratio was observed for all the BST compounds in this study, see Fig. 6. Although determination of the exact crossover pressure is challenging, and more detailed measurements in this pressure range are needed in order to fully elucidate the critical pressure for the crossover, no clear trend was observed with varying Sb concentration. Thus, we conclude that the appearance of the ETT is universal for BST compounds and independent of the Sb concentration. We note that in a previous study on Bi_2Te_3 [43], a noticeable change in the slope of resistivity around $\approx$ 4 GPa was observed, and this was associated to the existence of the ETT. In our electrical measurements results for BST-0.7, such a change of slope is not evident.

4.2 Effect of the Sb concentration on the critical pressure for the formation of the solid-solution BCC phase

The structural analysis of the BST compounds in this study clearly indicates the critical pressure for the formation of the BCC phase increases with increasing Sb concentration. In detail, for BST-0.2 the first sign for the appearance of the BCC phase is at 17.2 GPa,

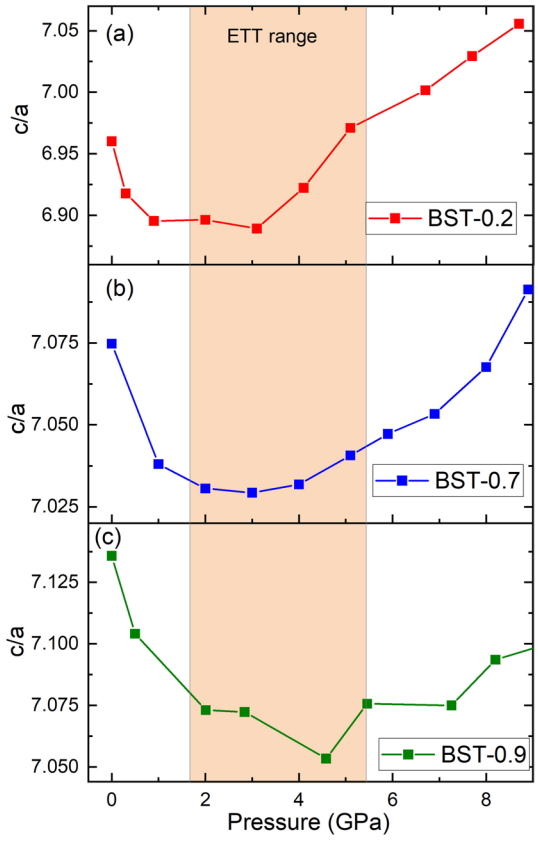

Fig. 6 *c/a* ratios of the $R-3m$ phase of **a**) BST-0.2, **b**) BST-0.7 and **c**) BST-0.9 as a function of pressure. The orange rectangle denotes the range of the ETT transition, see text. The solid lines are guides for the eye.

no BCC phase was observed for BST-0.7 up to 20 GPa, and for BST-0.9 BCC appears at 23.6 GPa, see Figs. 1 and 2. The observed trend is in agreement with that reported for pure Bi_2Te_3 (BST-0) [17, 18] and the corresponding observation of the BCC phase above 14.5 GPa. A previous study on Sb_2Te_3, with the appearance of BCC phase above 21.6 GPa [19], seems to contradict this trend. However, this apparent disagreement can be resolved considering that in Ref. [19], a 4:1 methanol-ethanol mixture was used as PTM, that is heavily non-hydrostatic above 12 GPa [24]. It is well known that non-hydrostatic conditions promote phase transitions to occur at lower pressures [44]. A similar trend could also be claimed for the formation of the $C2/c$ phase, see Fig. 2. However, the relatively small pressure differences and experimental limitations preclude a conclusion about a definite trend.

The trend discussed above, of increasing critical pressure for the formation of a solid-solution BCC phase upon increasing the Sb concentration, appears to be counterintuitive having in mind the Hume-Rothery rule that solid-solutions are promoted when atomic radii are close. Under ambient conditions, the atomic radius of Sb is closer (than that of Bi) to Te, and according to theoretical calculations, this continues to be valid under pressure [48, 49]. Thus, a plausible explanation is based on the well know trend under pressure, that isostructural compounds with smaller ions tend to have their pressure induced phase transitions shifted to higher pressures [50]. Larger ions exert a "chemical pressure" or "steric strain" on the structure.

4.3 Electrical properties under pressure

As mentioned in the results section, the transition from narrow-band-gap to → metallic character appears to occur at lower T upon pressure increase. This is in agreement with the general intuition that pressure promotes metallic character. Moreover, previous density functional theory (DFT) calculations [4] for the ambient conditions $R-3m$ phase of Bi_2Te_3, document that application of compressive strain along the *c*-axis results to an abrupt decrease of the band gap, eventually reaching metallization at ≈12 % compressive strain. Although a direct comparison with the present results under hydrostatic pressure is not possible, BST-0.7 undergoes a phase transition when the relative compression of the c-axis becomes higher than ≈5 % (see Fig. 3(b)) at ≈ 9 GPa, a common trend can be inferred. Most importantly, the aforementioned DFT calculations, predict a 3-fold decrease of the band gap, at ≈ 5% compressive strain, to values (50 meV) relevant with the thermal energy. This is in agreement with the experimental observation of a crossover between semiconducting and metallic behavior above 400 K at 2.5 and 5.3 GPa. Thus, the previous mentioned DFT calculations and present results do agree on the rapid decrease of the band gap under compression.

Moreover, according to previous DFT calculations under pressure [17], all the high-pressure phases of Bi_2Te_3 are metallic, in agreement with our experimental observation of a metallic sate above 12 GPa, *i.e.* above the first pressure-induced phase transition. The initial drop in the resistance at an earlier stage of pressure (< 5–6 GPa) can also be understood in terms of quick decrease in the carrier activation energy as reported for undoped Bi_2Te_3, albeit at different pressure [43, 51]. In general, carrier activation energy can be regarded as a measure of potential barriers. Upon compression with the decrease in carrier activation energy, the carriers are easier to be excited, ultimately resulting in decrease in resistance. Finally, we note that although attributing the crossover of the pressure dependence of the c/a axial ratio to an ETT transition looks reasonable, from our electrical measurements no direct effect on the electrical conductivity as a function of pressure was observed in the relevant pressure range. Indeed, the electrical conductivity shows a smooth variation between 2–8 GPa.

5 Conclusions

All the BST-x compounds (x=0.2, 0.7 and 0.9) investigated in this study exhibit identical structural evolution under pressure, that is also identical with the one for pure Bi_2Te_3 and Sb_2Te_3. Sb concentration marginally, if at all, affects critical pressures for the phase I → phase II → phase III phase transitions. However, increasing Sb concentration results to a clear increase of the critical pressure for the transition to the disordered BCC phase IV. The exact origin of this effect is still not clear. In the case of BST-0.7, the BCC phase was found to have an extensive pressure stability up to 180 GPa. For the same BST alloy, a pressure induced metallization was observed above 12 GPa. Finally, a clear crossover of the value of the c/a axial ratio of the ambient phase with increasing pressure, previously attributed to a pressure-induced ETT transition, was observed for all BST compounds of this study.

Supplementary Information

The online version contains supplementary material available at https://doi.org/10.1007/s43939-025-00309-4.

Supplementary file 1.

Acknowledgements
C.W. and S.F. acknowledge support from the Graduate Scholarships of the Guangdong Provincial Key Laboratory of Materials and Technologies for Energy Conversion. Y.A. would like to acknowledge generous support from the Pazy Research Foundation, Grant No. 398. The work performed at GTIIT was supported by funding from the Guangdong Technion Israel Institute of Technology and the Guangdong Provincial Key Laboratory of Materials and Technologies for Energy Conversion, MATEC (No. MATEC2022KF001). Beamline 12.2.2 at the Advanced Light Source is a DOE Office of Science User Facility under contract no. DE-AC02-05CH11231. Part of the synchrotron radiation experiments were performed at BL10XU of SPring-8 with the approval of the Japan Synchrotron Radiation Research Institute (JASRI) (Proposal Nos. 2024A1096 and 2024B1182). We also acknowledge DESY (Hamburg, Germany), a member of the Helmholtz Association HGF, for the provision of experimental facilities. Parts of this research were carried out at PETRA III beamline P02.2.

Author contributions
C.W. and E.S. wrote the main manuscript text with input from Y.A. C.W. and M.D. performed experimental measurements and analysis. W.L., H.Z., B.S., S.F. and Q.Z. performed measurements. M.D. and Z.S. synthesized the specimens. H.K., M.K. and B.W. provided methodology resources and experimental support. Y.A. and E.S. supervised the research, provided funding support and validated the results. All authors reviewed the manuscript.

Funding
The research was funded by Guangdong Technion Israel Institute of Technology, the Guangdong Provincial Key Laboratory of Materials and Technologies for Energy Conversion (MATEC2022KF001) and the Pazy Research Foundation (Grant No. 2032063).

Data availability
The data that support the findings of this study are available from the corresponding author upon reasonable request.

Declarations

Ethics approval and consent to participate
Not applicable.

Consent to publish
Not applicable.

Competing interests
The authors declare no competing interests.

Author details
[1]Materials Science and Engineering Department, Guangdong Technion-Israel Institute of Technology, Shantou 515063, China
[2]Department of Materials Science and Engineering, Technion-Israel Institute of Technology, Haifa 3200003, Israel
[3]Japan Synchrotron Radiation Research Institute, Sayo Hyogo 679-5198, Japan
[4]Advanced Light Source, Lawrence Berkeley National Laboratory, Berkeley 94720, California, USA
[5]Deutsches Elektronen-Synchrotron, DESY, Hamburg D-22603, Germany
[6]Guangdong Provincial Key Laboratory of Materials and Technologies for Energy Conversion, Guangdong Technion-Israel Institute of Technology, Shantou 515063, China

Received: 27 March 2025 / Accepted: 12 June 2025
Published online: 21 July 2025

References

1. Mansouri H, Sajjadi SA, Babakhani A, Saberi Y. Microstructure and thermoelectric performance evaluation of p-type $(Bi, Sb)_2Te_3$ materials synthesized using mechanical alloying and spark plasma sintering process. J Mater Sci Mater Electron. 2021;32:9858. https://doi.org/10.1007/s10854-021-05645-8.
2. Sun Y, Qin H, Zhang C, Wu H, Yin L, Liu Z, Guo S, Zhang Q, Cai W, Wu H, Guo F, Sui J. Sb_2Te_3 based alloy with high thermoelectric and mechanical performance for low-temperature energy harvesting. Nano Energy. 2023;107.
3. Mahan GD. Good Thermoelectrics, in *Solid State Physics*, series Solid State Physics, Vol. 51, edited by H. Ehrenreich and F. Spaepen (publisher Academic Press, 1998) pp. 81–157 https://doi.org/10.1016/S0081-1947(08)60190-3
4. Gayner C, Natanzon Y, Kauffmann Y, Amouyal Y. Topologically-enhanced thermoelectric properties in Bi_2Te_3-based compounds: effects of grain size and misorientation. ACS Appl Mater Interfaces. 2022;14:49730. https://doi.org/10.1021/acsami.2c12843.
5. Jacobsen MK, Kumar RS, Cornelius AL, Sinogeiken SV, Nico MF. High pressure x-ray diffraction studies of Bi_{2-x} Sb_x Te_3(x = 0,1,2). AIP Conf Proc. 2007;955:171. https://doi.org/10.1063/1.2833001.
6. Manjón FJ, Vilaplana R, Gomis O, Pérez-González E, Santamaría-Pérez D, Marín-Borrás V, Segura A, González J, Rodríguez-Hernández P, Muñoz A, Drasar C, Kucek V, Muñoz-Sanjosé V. High-pressure studies of topological insulators Bi_2se_3 , Bi_2Te_3, and Sb_2Te_3. Phys Status Solidi B. 2013;250:669. https://doi.org/10.1002/pssb.201200672.
7. Feutelais Y, Legendre B, Rodier N, Agafonov V. A study of the phases in the bismuth - tellurium system. Mater Res Bull. 1993;28:591. https://doi.org/10.1016/0025-5408(93)90055-I.
8. Nakajima S. The crystal structure of $Bi_2Sb_{3-x}Se_3$.J Phys Chem Solids. 1963;24:479. https://doi.org/10.1016/0022-3697(63)90207-5.

9. Hosokawa Y, Tomita K, Takashiri M. Growth of single-crystalline Bi2Te3 hexagonal nanoplates with and without single nanopores during temperature-controlled solvothermal synthesis. Sci Rep. 2019;9:10790. https://doi.org/10.1038/s41598-019-47356-5.
10. Ovsyannikov SV, Shchennikov VV, Vorontsov GV, Manakov AY, Likhacheva AY, Kulbachinskii VA. Giant improvement of thermoelectric power factor of Bi_2Te_3 under pressure. J Appl Phys. 2008;104. https://doi.org/10.1063/1.2973201.
11. Khvostantsev LG, Orlov AI, Abrikosov NKh, Svechnikova TE, Chizhevskaya SN. Thermoelectric properties and phase transitions in Bi_2Te_3 under hydrostatic pressure up to 9 GPa and temperature up to 300 C. Phys Status Solidi A. 1982;71:49.
12. Jacobsen MK, Sinogeikin SV, Kumar RS, Cornelius AL. High pressure transport characteristics of Bi_2Te_3, Sb_2Te_3 and $BiSb_2Te_3$. J Phys Chem Solids. 2012;73:1154. https://doi.org/10.1016/j.jpcs.2012.05.001.
13. Il'ina M, Itskevich E. Superconductivity of bismuth telluride at high pressure. Fiz Tverd Tela+ series Sverkhprovodimost' tellurida vismuta pod vysokim davleniem. 1975;17:154.
14. Zhu J, Zhang JL, Kong PP, Zhang SJ, Yu XH, Zhu JL, Liu QQ, Li X, Yu RC, Ahuja R, Yang WG, Shen GY, Mao HK, Weng HM, Dai X, Fang Z, Zhao YS, Jin CQ. Superconductivity in topological insulator Sb_2Te_3 induced by pressure. Sci Rep. 2013;3:2016. https://doi.org/10.1038/srep02016.
15. Zhang SJ, Zhang JL, Yu XH, Zhu J, Kong PP, Feng SM, Liu QQ, Yang LX, Wang XC, Cao LZ, Yang WG, Wang L, Mao HK, Zhao YS, Liu HZ, Dai X, Fang Z, Zhang SC, Jin CQ. The comprehensive phase evolution for Bi_2Te_2topological compound as function of pressure. J Appl Phys. 2012;111.
16. Einaga M, Tanabe Y, Nakayama A, Ohmura A, Ishikawa F, Yamada Y. New superconducting phase of Bi_2Te_3 under pressure above 11 GPa. J Phys Conf Ser. 2010;215. https://doi.org/10.1088/1742-6596/215/1/012036.
17. Zhu L, Wang H, Wang Y, Lv J, Ma Y, Cui Q, Ma Y, Zou G. Substitutional alloy of Bi and Te at high pressure. Phys Rev Lett. 2011;106: 145501. https://doi.org/10.1103/PhysRevLett.106.145501.
18. Einaga M, Ohmura A, Nakayama A, Ishikawa F, Yamada Y, Nakano S. Pressure-induced phase transition of Bi_2Te_3 to a bcc structure. Phys Rev B. 2011;83. https://doi.org/10.1103/PhysRevB.83.092102.
19. Ma Y, Liu G, Zhu P, Wang H, Wang X, Cui Q, Liu J, Ma Y. Determinations of the high-pressure crystal structures of Sb_2Te_3. J Phys Condens Matter. 2012;24.
20. Souza SM, Poffo CM, Trichês DM, de Lima JC, Grandi TA, Polian A, Gauthier M. High pressure monoclinic phases of Sb_2Te_3. Phys B Condens Matter. 2012;407:3781. https://doi.org/10.1016/j.physb.2012.05.061.
21. Bai F-X, Yu H, Peng Y-K, Li S, Yin L, Huang G, Chen L-C, Goncharov AF, Sui J-H, Cao F. Electronic topological transition as a route to improve thermoelectric performance in $Bi_{0.5}$ $Sb_{1.5}$ Te_3. Adv Sci. 2022;9:2105709.
22. Syassen K. Ruby under pressure. High Pressure Res. 2008;28:75. https://doi.org/10.1080/08957950802235640.
23. Anderson OL, Isaak DG, Yamamoto S. Anharmonicity and the equation of state for gold. J Appl Phys. 1989;65:1534.
24. Klotz S, Chervin J-C, Munsch P, Le Marchand G. Hydrostatic limits of 11 pressure transmitting media. J Phys D Appl Phys. 2009;42: 075413. https://doi.org/10.1088/0022-3727/42/7/075413.
25. Kunz M, MacDowell AA, Caldwell WA, Cambie D, Celestre RS, Domning EE, Duarte RM, Gleason AE, Glossinger JM, Kelez N. A beamline for high-pressure studies at the advanced light source with a superconducting bending magnet as the source. J Synchrotron Radiat. 2005;12:650.
26. Hirao N, Kawaguchi SI, Hirose K, Shimizu K, Ohtani E, Ohishi Y. New developments in high-pressure X-ray diffraction beamline for diamond anvil cell at SPring-8. Matter Radiat at Extremes. 2020;5: 018403. https://doi.org/10.1063/1.5126038.
27. Prescher C, Prakapenka VB. DIOPTAS: a program for reduction of two-dimensional X-ray diffraction data and data exploration. High Pressure Res. 2015;35:223.
28. Kraus W, Nolze G. POWDER CELL–a program for the representation and manipulation of crystal structures and calculation of the resulting X-ray powder patterns. J Appl Crystallogr. 1996;29:301.
29. Boultif A, Louër D. Powder pattern indexing with the dichotomy method. J Appl Crystallogr. 2004;37:724.
30. Toby BH, Von Dreele RB. GSAS-II: the genesis of a modern open-source all purpose crystallography software package. J Appl Crystallogr. 2013;46:544.
31. Birch F. Finite strain isotherm and velocities for single-crystal and polycrystalline NaCl at high pressures and 300k. J Geophys Res Solid Earth. 1978;83:1257.https://doi.org/10.1029/JB083iB03p01257.
32. Ono S. The equation of state of B2-type NaCl. J Phys Conf Ser. 2010;215: 012196. https://doi.org/10.1088/1742-6596/215/1/012196.
33. Sakai T, Ohtani E, Hirao N, Ohishi Y. Equation of state of the NaCl-B2 phase up to 304 GPa. J Appl Phys. 2011;109: 084912. https://doi.org/10.1063/1.3573393.
34. Chen X, Ma Y. High-pressure structures and metallization of sodium chloride. Europhys Lett. 2012;100:26005. https://doi.org/10.1209/0295-5075/100/26005.
35. Mao HK, Hemley RJ, Chen LC, Shu JF, Finger LW, Wu Y. X-ray diffraction to 302 gigapascals: high-pressure crystal structure of cesium iodide. Science. 1989;246:649. https://doi.org/10.1126/science.246.4930.649.
36. Mao HK, Wu Y, Hemley RJ, Chen LC, Shu JF, Finger LW, Cox DE. High-pressure phase transition and equation of state of CsI. Phys Rev Lett. 1990;64:1749. https://doi.org/10.1103/PhysRevLett.64.1749.
37. Akahama Y, Kawamura H, Singh AK. Equation of state of bismuth to 222 GPa and comparison of gold and platinum pressure scales to 145 GPa. J Appl Phys. 2002;92:5892. https://doi.org/10.1063/1.1515378.
38. Akahama Y, Okawa N, Sugimoto T, Fujihisa H, Hirao N, Ohishi Y. Coexistence of a metastable double hcp phase in bcc–fcc structure transition of Te under high pressure. Jpn J Appl Phys. 2018;57: 025601. https://doi.org/10.7567/JJAP.57.025601.
39. Degtyareva O, MCMahon MI, Nelmes RJ. High-pressure structural studies of group-15 elements. High Pressure Res. 2004;24:319. https://doi.org/10.1080/08957950412331281057.
40. Magad-Weiss LK, Adeleke AA, Greenberg E, Prakapenka VB, Yao Y, Stavrou E. High-pressure structural study of a-mn: experiments and calculations. Phys Rev B. 2021;103.
41. Dawod M, Amouyal Y et al. To be submitted
42. Lu W, Zhang L, Wei C, Zhang Q, Kunz M, Kawaguchi S, Kadobayashi H, Boussard-Plèdel C, Bureau B, Jiang J, Ahmad AS, Ein-Eli Y, Stavrou E. Pressure-induced crystallization and metallization in glassy As_{20} Se_{80}. Phys Rev B. 2025;111. https://doi.org/10.1103/PhysRevB.111.024115.
43. Zhang J, Liu C, Zhang X, Ke F, Han Y, Peng G, Ma Y, Gao C. Electronic topological transition and semiconductor-to-metal conversion of Bi_2Te_3under high pressure. Appl Phys Lett. 2013;103. https://doi.org/10.1063/1.4816758.

44. Zhang X, Dai L, Hu H, Hong M, Li C. Pressure-induced reversible structural phase transitions and metallization in GeTe under hydrostatic and non-hydrostatic environments up to 22.9 GPa. J Non-Cryst Solids. 2023;618: 122516.
45. Cheng H, Yao H, Xu Y, Jiang J, Yang Y, Wang J, Li X, Li Y, Shao J. Pressure-induced alloying and superconductivity in GeTe. Chem Mater. 2024;36:3764. https://doi.org/10.1021/acs.chemmater.4c00087.
46. Polian A, Gauthier M, Souza SM, Trichês DM, Cardoso de Lima Ja, Grandi TA. Two-dimensional pressure-induced electronic topological transition in Bi_2Te_3. Phys Rev B. 2011;83: 113106. https://doi.org/10.1103/PhysRevB.83.113106.
47. Nakayama A, Einaga M, Tanabe Y, Nakano S, Ishikawa F, Yamada Y. Structural phase transition in Bi_2Te_3 under high pressure. High Pressure Res. 2009;29:245. https://doi.org/10.1080/08957950902951633.
48. Rahm M, Hoffmann R, Ashcroft NW. Atomic and ionic radii of elements 1–96. Chemistry– A European Journal. 2016;22:14625. https://doi.org/10.1002/chem.201602949.
49. Rahm M, Ångqvist M, Rahm JM, Erhart P, Cammi R. Non-bonded radii of the atoms under compression. ChemPhysChem. 2020;21:2441. https://doi.org/10.1002/cphc.202000624.
50. Bassett WA, Takahashi T, Mao H, Weaver JS. Pressure-induced phase transformation in NaCl. J Appl Phys. 1968;39:319. https://doi.org/10.1063/1.1655752.
51. Zhang JL, Zhang SJ, Weng HM, Zhang W, Yang LX, Liu QQ, Feng SM, Wang XC, Yu RC, Cao LZ, Wang L, Yang WG, Liu HZ, Zhao WY, Zhang SC, Dai X, Fang Z, Jin CQ. Pressure-induced superconductivity in topological parent compound Bi_2Te_3. Proc Natl Acad Sci. 2011;108:24. https://doi.org/10.1073/pnas.1014085108.

Publisher's Note